Supporting information

Magnetism-induced huge enhancement of room-temperature thermoelectric and cooling performance of p-type BiSbTe alloys

Cuncheng Li[1], Shifang Ma[1], Ping Wei[1,2], Wanting Zhu[1], Xiaolei Nie[1], Xiahan Sang[1,2], Zhigang Sun[1], Qingjie Zhang[1] and Wenyu Zhao[1*]

[1]*State Key Laboratory of Advanced Technology for Materials Synthesis and Processing, Wuhan University of Technology, Wuhan 430070, China*

[2]*Nanostructure research center, Wuhan University of Technology, Wuhan 430070, China*

*e-mail: wyzhao@whut.edu.cn

1. Measuring direction of electrical and thermal transport properties

The test directions of transport properties are shown in **Fig. S1.** All transport properties were measured along the in-plane direction (perpendicular to the pressure axis).

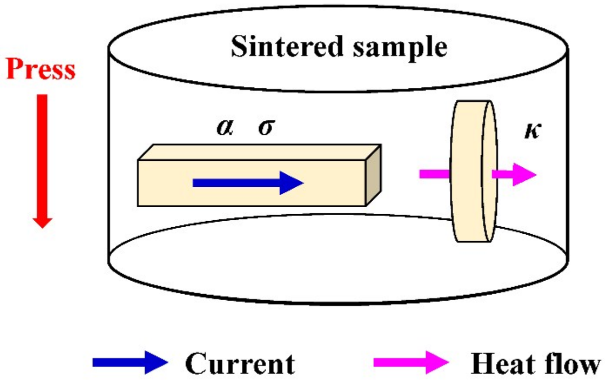

Fig. S1 Schematic diagram direction for measuring the electrical and thermal transport properties

2. Heat capacities of MNC00 and MNC15 in the range of 300-465 K

To examine whether the heat capacity (C_p) is changed after introducing Fe_3O_4-NPs, the C_p values of MNC00 and MNC15 were measured by DSC in the range of 300-465 K and the results are shown in **Fig. S2**. It can be seen that the C_p of MNC00 is about 0.18 J·g^{-1}·K^{-1} at 300 K. There is no apparent difference in heat capacities of MNC00 and MNC15.

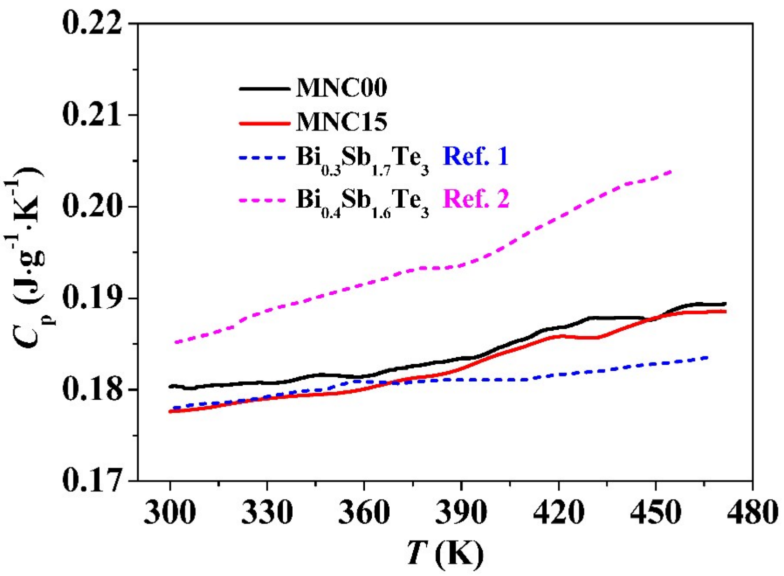

Fig. S2 Heat capacities of MNC00 and MNC15 in the range of 300-465 K

3. The distribution of Fe_3O_4-NPs in $Fe_3O_4/Bi_{0.5}Sb_{1.5}Te_3$ nanocomposite bulk materials

Fig S3 shows the secondary electron image (SEI) of a micro-area and its corresponding back-scattered electron image (BEI). It can be seen that the positions of black contrasts in BEI correspond well with those of black contrasts in SEI. The mapping image of Fe element (**Fig. S3c**) in the micro-area also coincides very well with those of black contrasts. These results clearly show that the black contrasts in SEI and BEI are the distribution of Fe_3O_4 nanoparticles.

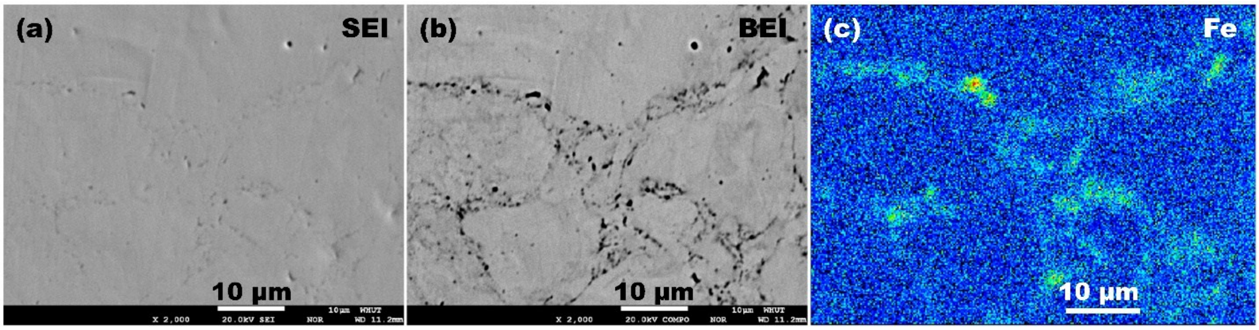

Fig. S3 EPMA analysis of polished surface of MNC15 sample. (a) Secondary electron image SEI. (b) Back-scattered electron image BEI. (c) Mapping image of Fe element obtained by wavelength-dispersive spectrometer.

4. The agglomeration state of Fe_3O_4-NPs in our materials

Experimentally, the preparation of monodispersed Fe_3O_4-NPs is not a difficult thing if enough organic dispersants are used. However, we discover that too many organic dispersants may cause the remarkable reduction in the thermoelectric and cooling performance. We have carefully investigated the microstructure characterization of synthesized Fe_3O_4-NPs, as-prepared $Fe_3O_4/Bi_{0.5}Sb_{1.5}Te_3$ nanocomposite powders and SPSed $Fe_3O_4/Bi_{0.5}Sb_{1.5}Te_3$ nanocomposite bulk materials. As shown in **Fig. S4a** and **S4b**, the synthesized Fe_3O_4-NPs are 9-18 nm in size and their crystal structure is consistent with the cubic spinel phase, having been aggregated because of the high surface energy and strong magnetic dipole-dipole attractions[3]. It can be seen that plenty of Fe_3O_4-NPs with 30~110 nm in size are randomly dispersed on the surfaces of as-prepared $Fe_3O_4/Bi_{0.5}Sb_{1.5}Te_3$ nanocomposite powders as shown in **Fig. S4c**. The surface of SPSed $Bi_{0.5}Sb_{1.5}Te_3$ matrix bulk material is very clean (**Fig. S4d**). The as-prepared $Fe_3O_4/Bi_{0.5}Sb_{1.5}Te_3$ nanocomposite powders have been sintered into SPSed $Fe_3O_4/Bi_{0.5}Sb_{1.5}Te_3$ nanocomposite bulk materials (**Fig. S4e**). The sizes of Fe_3O_4-NPs in **Fig. S4c** and **Fig. S4e** are almost the same, implying that Fe_3O_4-NPs have not grown up during the SPS process. It can be seen from **Fig. S4f** as well as **Figure 2d** and **Figure 3** that Fe_3O_4-NPs in fact consist of fine nanoparticles with a diameter of 9-18 nm. These microstructures show that our preparation process may keep fine Fe_3O_4-NPs in soft agglomeration state all the time. Namely, Fe_3O_4-NPs embedded into $Bi_{0.5}Sb_{1.5}Te_3$ matrix may be in superparamagnetic state and can generate carrier multiple scattering effect.

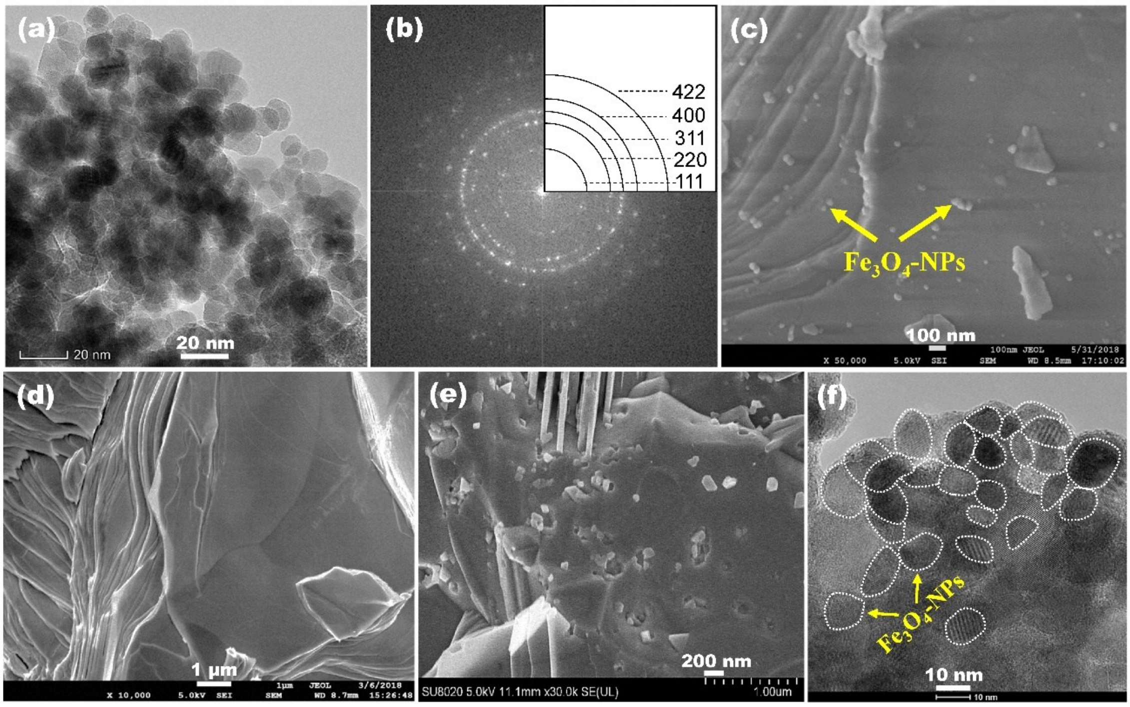

Fig. S4 (a) HRTEM image of synthesized Fe_3O_4-NPs. (b) Corresponding selected area electron diffraction (SAED) pattern of (a). FESEM images of (c) nanocomposite powders (x=0.15%), (d) fracture surface of SPSed matrix, (e) fracture surface of SPSed nanocomposite material. (f) TEM image of MNC15.

5. Magnetic transition of Fe_3O_4-NPs based on theoretical calculation

I. Ferromagnetism-superparamagnetism transition

Superparamagnetism is that the magnetic moment of single-domain particles begins to randomly fluctuate when the thermal energy (k_BT) overcomes the anisotropic energy (K_1V). Therefore, we can roughly calculate the critical diameter (D) of magnetic particles to undergoing the superparamagnetic transition under different temperature by

$$k_BT = K_1V \qquad (1)$$

$$V = \frac{\pi D^3}{6} \qquad (2)$$

where k_B, K_1, V, and D is Boltzmann constant, anisotropy constant, volume and diameter of spherical particles, respectively. Using the data from ref. 4-6, we can calculate the K_1 of Fe_3O_4-NPs. As a result, the temperature dependence of D is calculated and the result is shown in **Fig.S5a.**

II. Ferromagnetism-paramagnetism transition

The ferromagnetic nanoparticles could undergo another magnetic transition from ferromagnetism to paramagnetism. According to a size-dependent cohesive-energy model reported previously[7], the transition temperature or Curie temperature (T_C) can be expressed as

$$\frac{T_c(D)}{T_c(\infty)} = \left\{1 - \frac{1}{[2D/(ch)]-1}\right\} exp\left\{-\frac{2S_b}{3R}\frac{1}{[2D/(ch)]-1}\right\} \qquad (3)$$

where '∞' is the bulk value and T_c (∞) = 860 K for Fe_3O_4; R= 8.314 J mol^{-1} K^{-1}; S_b denotes the bulk evaporation entropy of crystals (S_b=13 R); h is 0.2220 nm for Fe_3O_4 and c=1 for nanoparticles. [7] Using these parameters, the corresponding D of T_C has been calculated and the results are shown in **Fig.S5b.**

According to the results from theoretical calculation above, we can conclude that the as-prepared Fe_3O_4-NPs with an average diameter of 9.8 nm would remain superparamagnetic state in the whole temperature range of 300-500 K.

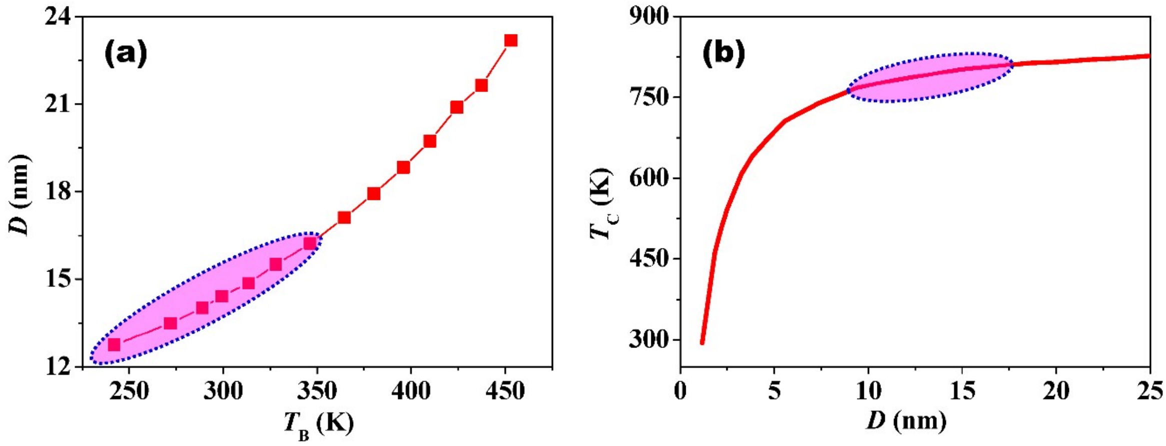

Fig. S5 Theoretical calculation of magnetic transformation of Fe_3O_4-NPs. (a) Blocking temperature T_B dependence of critical diameter D. (b) D dependence of Curie temperature T_C.

6. Temperature-dependent mobility curves in the range of 50-300 K

The temperature-dependent mobility curves of MNC00, MNC05, MNC10 and MNC15 were measured in the range of 50-300 K and the results are displayed in **Fig. S6**. We fitted the mobility above the blocking temperature (T_B = 210 K) of Fe_3O_4 nanoparticles according to the power law $T^{-\lambda}$. The λ of these samples with x = 0, 0.05%, 0.10% and 0.15% is 1.85, 1.86, 1.88 and 1.92, respectively. The increase of λ means the enhanced carrier scattering after adding superparamagnetic Fe_3O_4 nanoparticles. This is why the mobility is not significantly increased on the condition that the carrier concentration is decreased for $Fe_3O_4/Bi_{0.5}Sb_{1.5}Te_3$ nanocomposite.

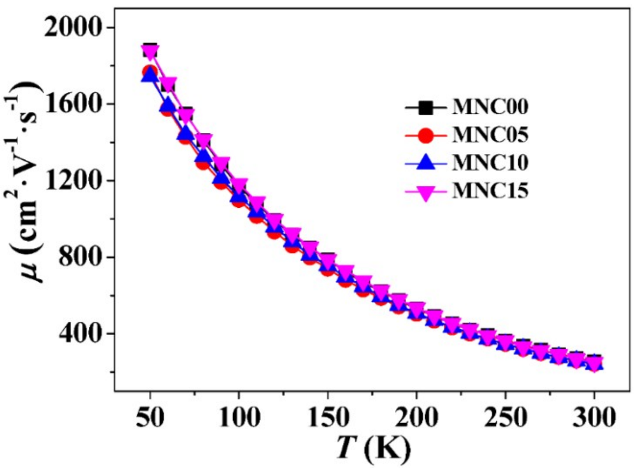

Fig. S6 Temperature-dependent mobility curves of MNC00, MNC05, MNC10 and MNC15 samples in the range of 50-300 K

7. Effective mass of MNC00 at 300 K

The carrier concentration at 300 K has been affected by the minority carriers. It would be more convincing to calculate the effective mass by the low-temperature carrier concentration. The carrier concentrations of MNC00 in the range of 200-300 K were measured with PPMS and the result is shown in **Fig. S7**. It can be seen that the variation in carrier concentration is not significant. We choose the carrier concentration at 250 K and the Seebeck coefficient at 300 K to calculate the effective mass m^*. The calculated m^* is about 1.12 m_0.

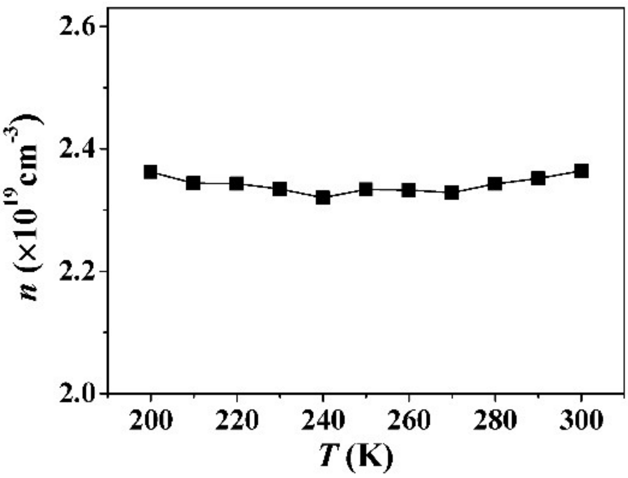

Fig. S7 Carrier concentrations of MNC00 in the range of 200-300 K

8. Repeatability of the thermoelectric performance for MNC15

To demonstrate the high stability and cyclability for materials, the in-plane transport properties of MNC15 were repeatedly measured for five times in the range 300-500 K, and the results are shown in **Fig. S8**. It can be seen that the deviations of all the parameters are very small, substantiating the good stability and cyclability. The maximum *ZT* values are very close to reported data 1.5.

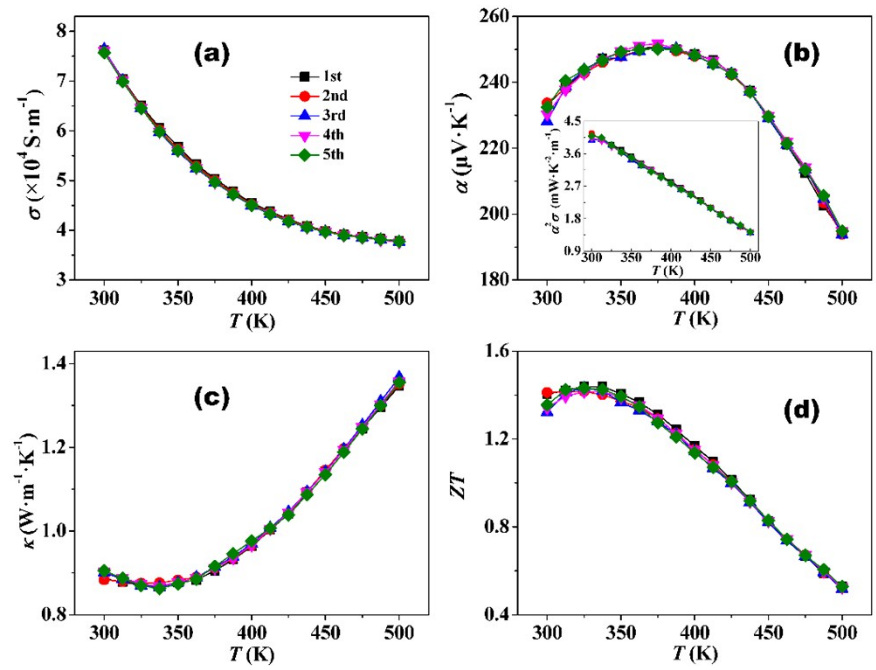

Fig.S8 Temperature dependence of transport properties for MNC15. (a) Electrical conductivity. (b) Seebeck coefficient. Insert is the power factor. (c) Thermal conductivity. (d) *ZT* value.

9. Anisotropic thermoelectric properties of MNC15

To investigate the anisotropic thermoelectric properties of MNC15, we measured the transport properties along the out-of-plane and in-plane directions. As can be seen form **Fig. S9**, the Seebeck coefficient along two directions are almost same but the electrical and thermal conductivities exhibit obviously anisotropic characteristics. The σ_{in}/σ_{out} and κ_{in}/κ_{out} ratios at 300 K are 1.58 and 1.26, respectively. The maximum *ZT* values are about 1.5 (340 K) and 1.2

(350 K) along the in-plane and out-of-plane directions, respectively.

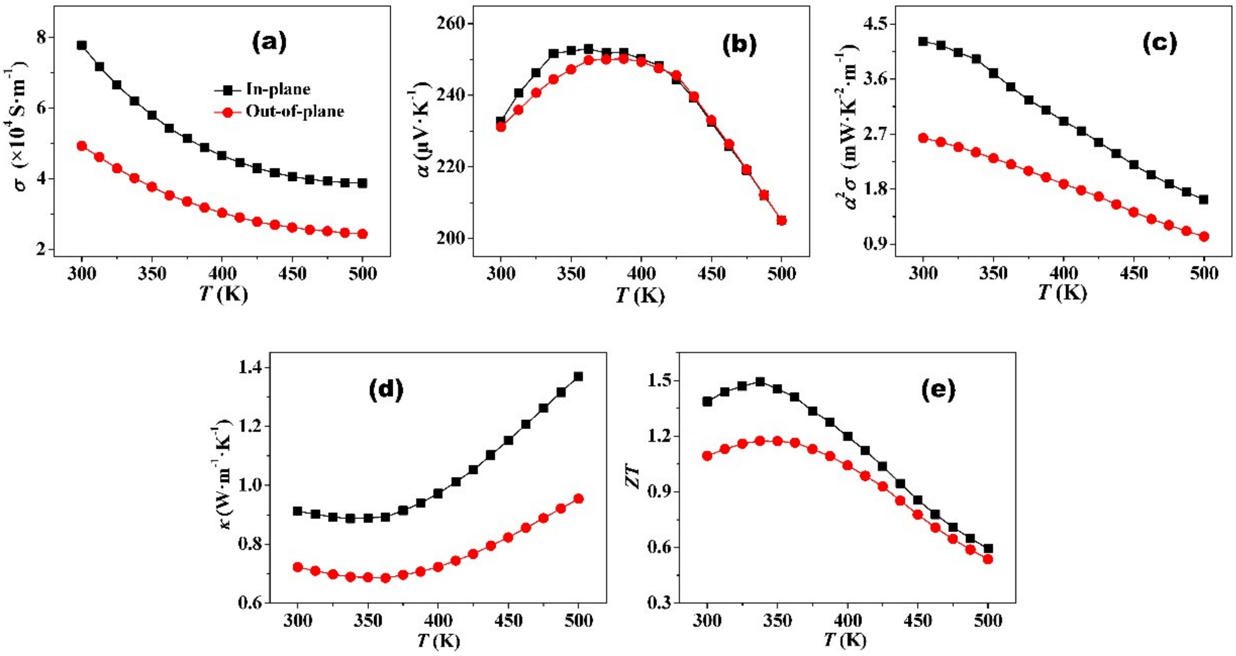

Fig. S9 Transport properties of MNC15 along the in-plane and out-of-plane directions in the range of 300-500 K. (a) Electrical conductivity. (b) Seebeck coefficient. (c) Power factor. (d) Thermal conductivity. (e) Dimensionless figure of merit *ZT*.

10. Infrared images of MNC00D and MNC15D under cooling working model

Fig. S10 shows the infrared (IR) images of cooling MNC00D (a-e) and MNC15D (f-j) under different working currents. It can be seen that with the increase of working current (I), the heating-side temperature (T_h) of both devices increases monotonically, and the cooling-side temperature (T_c) first decreases and then rises. The threshold current to obtained the lowest T_c are 0.6 A and 1.0 A for MNC00D and MNC15D, respectively.

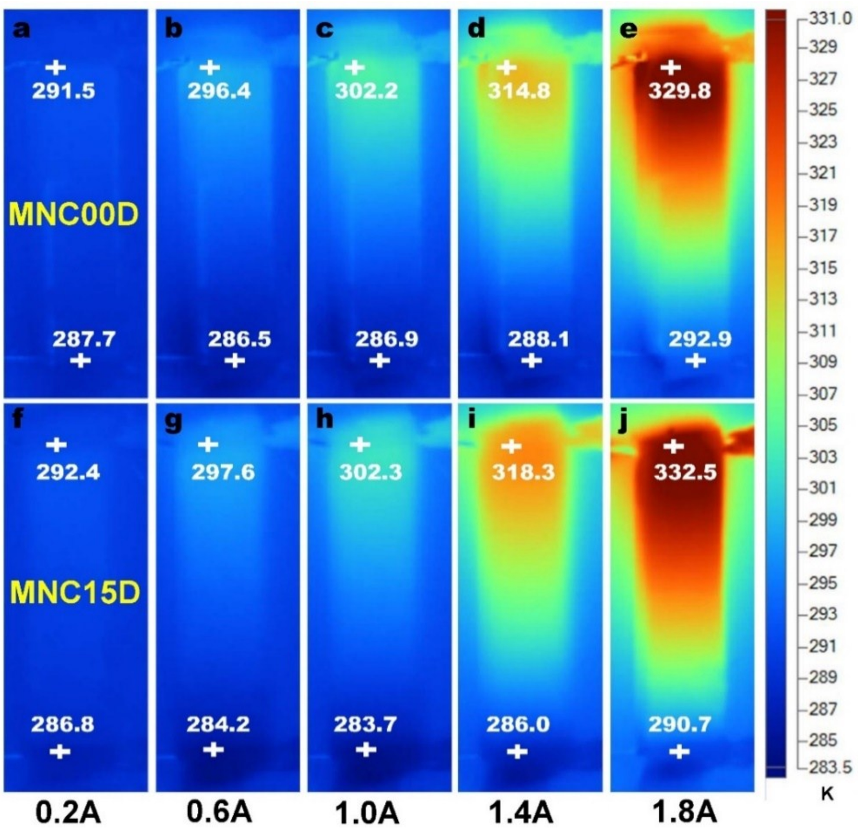

Fig. S10 IR images under different working currents. (a)-(e) T_h and T_c of MNC00D. (f)-(j) T_h and T_c of MNC15D.

11. Stability and cyclability of cooling performance for MNC15D

In order to investigate the stability and cyclability of cooling performance for MNC15D, the cooling performance have been re-measured for ten times at room temperature (T_r = 291.8 K) under 1.0 A and 1.8 A, respectively. As shown in **Fig. S11**, all curves shows very high repeatability. The specific values are listed in **Table S1**.

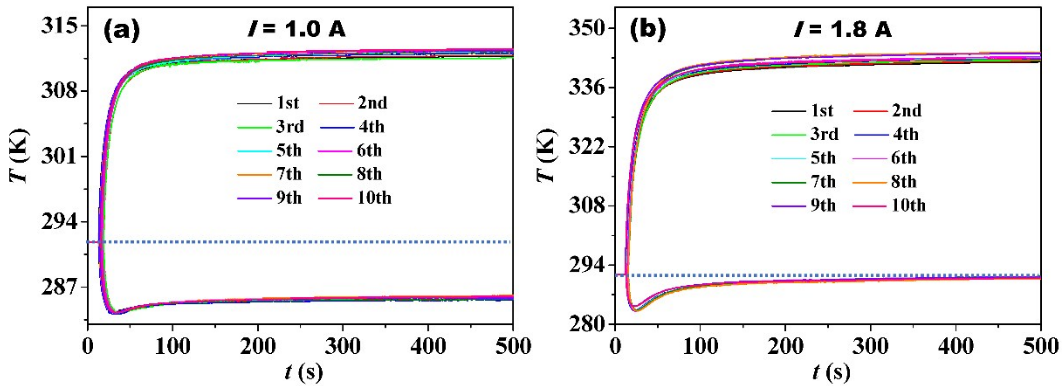

Fig. S11 Stability and cyclability of cooling performance of device MNC15D. Time dependence of T_h and T_c under (a) 1.0 A and (b) 1.8 A.

Table S1 Stability and cyclability test under 1.0 A and 1.8 A

	I = 1.0 A				I = 1.8 A			
Number	T_h (K)	T_c (K)	ΔT_{c15} (K)	ΔT_{15} (K)	T_h (K)	T_c (K)	ΔT_{c15} (K)	ΔT_{15} (K)
1	311.7	285.7	6.1	26.0	342.1	290.9	0.9	51.2
2	311.8	285.7	6.1	26.1	342.3	290.9	0.9	51.4
3	311.6	285.8	6.0	25.8	342.5	291.0	0.8	51.5
4	312.1	285.7	6.1	26.4	342.8	291.0	0.8	51.8
5	312.2	285.9	5.9	26.3	343.1	291.2	0.6	51.9
6	312.4	286.0	5.8	26.4	343.3	290.9	0.9	52.4
7	312.5	286.1	5.7	26.4	344.1	291.4	0.4	52.7
8	312.2	285.7	6.1	26.5	344.3	290.8	1.0	53.5
9	312.5	286.0	5.8	26.5	344.0	291.2	0.6	52.8
10	312.3	285.8	6.0	26.5	342.9	290.8	1.0	52.1

Note: The ΔT is the working temperature difference between T_h and T_c while the ΔT_c represents the cooling temperature difference between T_c and T_r. Subscripts 15 represents the device made with MNC15.

Reference

1. J. H. Li, Q. Tan, J. F. Li, D. W. Liu, Fu Li, Z. Y. Li, M. M. Zou and K. Wang, *Adv. Funct. Mater.*, 2013, **23**, 4317–4323.
2. Y. Y. Li, X. Y. Qin, D. Li, J. Zhang, C. Li, Y. F. Liu, C. J. Song, H. X. Xin and H. F. Guo, *Appl. Phys. Lett.*, 2016, **108**, 062104.
3. G. Li, Y. Jiang, K. Huang, P. Ding and J. Chen, *J. Alloys Compd.,* 2008, **466**, 451-456.
4. R. Reznicek, V. Chlan, H. Stepankova, P. Novak and M. Marysko, *J. Phys. Condens. Matter.*, 2012, **24**, 055501.
5. Z. Kakol and J. M. Honig, *Phys. Rev. B*, 1989, **40**, 9090-9097.
6. E. M. Gyorgy and H. M. O'Bryan JR, *Phys. Lett.*, 1966, **23**, 513-514.
7. C. C. Yang and Q. Jiang, *Acta Mater.*,2005, **53**, 3305–3311.